



<b>Title</b>	<b>Molybdenum Disulfide-Coated Lithium Vanadium Fluorophosphate Anode: Experiments and First-Principles Calculations</b>
<b>Author(s)</b>	<b>Liu, Z; Peng, W; Xu, Z; Shih, K; Wang, JJ; Wang, Z; Lv, X; Chen, J; Li, X</b>
<b>Citation</b>	<b>ChemSusChem, 2016, v. 9 n. 16, p. 2122-2128</b>
<b>Issued Date</b>	<b>2016</b>
<b>URL</b>	<b><a href="http://hdl.handle.net/10722/234529">http://hdl.handle.net/10722/234529</a></b>
<b>Rights</b>	<b>This is the accepted version of the following article: ChemSusChem, 2016, v. 9 n. 16, p. 2122-2128, which has been published in final form at <a href="http://onlinelibrary.wiley.com/wo1/doi/10.1002/cssc.201600370/aabstract">http://onlinelibrary.wiley.com/wo1/doi/10.1002/cssc.201600370/aabstract</a>; This work is licensed under a Creative Commons Attribution-NonCommercial-NoDerivatives 4.0 International License.</b>

# **Molybdenum disulfide decorating lithium vanadium fluorophosphate for lithium ion batteries anode: Experiments and first-principles calculations**

Zhaomeng Liu,<sup>a</sup> Wenjie Peng,<sup>a</sup> Zhenming Xu,<sup>a</sup> Kaimin Shih,<sup>b</sup> Jiexi Wang,<sup>a,b,\*</sup> Zhixing Wang,<sup>a</sup>  
Xiaojun Lv,<sup>a</sup> Jiangan Chen,<sup>c</sup> Xinhai Li<sup>a</sup>

<sup>a</sup> School of Metallurgy and Environment, Central South University, 932, Lushan South Road, Changsha, P.R. China, 410083.

<sup>b</sup> Department of Civil Engineering, The University of Hong Kong, Hong Kong.

<sup>c</sup> Faculty of Resource and Environmental Engineering, Jiangxi University of Science and Technology, Ganzhou 341000, China.

\* Corresponding author, [wangjiexikeen@csu.edu.cn](mailto:wangjiexikeen@csu.edu.cn); [jxwang@hku.hk](mailto:jxwang@hku.hk).

**ABSTRACT:** To develop a novel anode material and therefore meet the increasing demands of lithium-ion battery, for the first time, MoS<sub>2</sub> is employed to modify LiVPO<sub>4</sub>F anode to improve its lithium storage performance at 3~0.01 V. Morphological observations presents that the MoS<sub>2</sub>-modified LiVPO<sub>4</sub>F particles (M-LVPF) are wrapped by amorphous carbon as interlayer and layered MoS<sub>2</sub> as outer layer. Charge-discharge tests show M-LVPF delivers a high reversible capacity of 308 mAh g<sup>-1</sup> at 50 mA g<sup>-1</sup>. After cycled at 1.0 A g<sup>-1</sup> for 300 times, it maintains 98.7% capacity retention. Moreover, it exhibits high rate capability with a specific capacity of 199 mAh g<sup>-1</sup> at 1.6 A g<sup>-1</sup>. EIS tests indicate the lithium ion diffusion and charge-exchange reaction at the surface of M-LVPF are greatly enhanced. First-principles calculations demonstrate that the process of MoS<sub>2</sub> absorbing on LiVPO<sub>4</sub>F is exothermic and spontaneous, and the electron transfer property of the MoS<sub>2</sub>-absorbed LiVPO<sub>4</sub>F surface is enhanced.

**KEYWORDS:** lithium vanadium fluorophosphates; molybdenum disulfide; surface modification; first-principle calculation

## Introduction

To achieve the increasing demands for the energy systems of pure or hybrid electric vehicles, it is very important to establish a sustainable and efficient energy solution.<sup>[1]</sup> Li-ion batteries (LIBs) have aroused huge interest around the world owing to their high energy density and design flexibility.<sup>[2]</sup> As one of the crucial components, anode material plays an important role in affecting the performance of LIBs.<sup>[3]</sup> Among the developed anode materials, carbonaceous materials (especially graphite) have been used as main anodes for commercial LIBs. However, graphite exhibits poor rate capability and cycling performance due to its low Li<sup>+</sup> diffusion coefficient. Moreover, it suffers serious safety issue because of the deposition of dendritic lithium on the surface of anode at low

potential.<sup>[4]</sup> To develop the candidates for commercial graphite, conversion-type<sup>[5]</sup> (e.g., transition metal oxides/sulfides) and alloy-type<sup>[6]</sup> (e.g., Si, Sn) anode materials have been widely investigated. However, these materials suffer from large volume change during the charge-discharge process. In addition, for transition metal oxides, the problem of voltage hysteresis makes it hard for practical applications. Therefore, it is still a challenge to seek for new anode materials with high good cycle stability and superior rate capability.

**Triclinic** LiVPO<sub>4</sub>F has been widely investigated as the cathode material because of its high operating voltage and excellent thermal stability.<sup>[7]</sup> Interestingly, due to an additional lithium insertion reaction at around 1.8 V associated with the V<sup>2+</sup>/V<sup>3+</sup> redox couple, LiVPO<sub>4</sub>F was also studied as a potential anode material.<sup>[8]</sup> The theoretical specific capacity based on this insertion reaction is 156 mAh g<sup>-1</sup>. However, LiVPO<sub>4</sub>F anode has been reported to deliver unacceptable cycling performance and rate capability caused by poor electronic conductivity and slightly irreversible structural evolution.<sup>[8a, 9]</sup> Up to now, very limited researches pay attention to improving the performance of LiVPO<sub>4</sub>F anode. Our previous work **showed** that decreasing the discharge cut-off potential is able to increase the capacity of LiVPO<sub>4</sub>F, attributed to the extra lithium ion storage ability deriving from the conversion reaction at low potential. Moreover, the electrochemical performance of LiVPO<sub>4</sub>F was also enhanced by graphene coating and decreasing the cut-off discharge potential.<sup>[8b]</sup> However, the performance of LiVPO<sub>4</sub>F anode is still not satisfied and further improvement is urgently needed.

Recently, layered molybdenum disulfide (MoS<sub>2</sub>) has received increasing attentions because of its unique physical and chemical properties such as high surface area, excellent structural flexibility and good conductivity.<sup>[10]</sup> Given the analogous structure of

graphene, MoS<sub>2</sub> has great potential for serving as a dressing agent to provide efficient electrical/ionic pathways for LiVPO<sub>4</sub>F anode. Moreover, MoS<sub>2</sub> itself is a conversion-type anode material with high capacity, which is able to contribute to the capacity resultant coated materials.

Herein, we report MoS<sub>2</sub> coating to improve the performance of LiVPO<sub>4</sub>F anode for the first time. The MoS<sub>2</sub>-coated LiVPO<sub>4</sub>F anode material (M-LVPF) is investigated via both experiments and first-principles calculations. Due to the high surface area and structural flexibility, MoS<sub>2</sub> nanosheets can effectively coat on the surface of the nanosized LiVPO<sub>4</sub>F particles through a facile solution method. By calculating the adsorption energy and electronic structure of the MoS<sub>2</sub>-adsorbed LiVPO<sub>4</sub>F surface, the functions of MoS<sub>2</sub> in this core/shell structure would be clearly explained. We expect the MoS<sub>2</sub>-coated LiVPO<sub>4</sub>F composite will show an improved electrochemical performance.

## **Experimental section**

### **Synthesis of MoS<sub>2</sub> wrapped LiVPO<sub>4</sub>F nanocomposite**

LiVPO<sub>4</sub>F nanoparticles were prepared as described in previous literature.<sup>[11]</sup> The MoS<sub>2</sub> powders were synthesized by a one-step hydrothermal method.<sup>[10a]</sup> The synthetic process of M-LVPF composite was as follows. Firstly, 0.035 g well-prepared MoS<sub>2</sub> powders were dissolved in 50 mL ethanol under strongly stirring for 2 h with the assistance of ultrasonic wave. After that, 2.0 g high-crystallinity LiVPO<sub>4</sub>F/C was added into as-prepared MoS<sub>2</sub> dispersion with magnetic stirring at the constant temperature of 85 °C until the water was completely evaporated. The obtained slurry was dried in the oven at 120 °C for 6 h. Finally, the dried large aggregation was thoroughly grinded in an agate mortar and then sintered at 400 °C for 4 h in a tube furnace in an argon atmosphere. The mass content of MoS<sub>2</sub> in the prepared coated sample was 1.75 wt.%.

## Materials Characterization

The as-prepared samples were characterized by X-ray diffraction (XRD, Rint-2000, Rigaku, Japan). The morphologies were delivered by scanning electron microscope (FESEM, FEI Quanta-250) and transmission electron microscope (TEM, Tecnai G12, 200 kV). The mass contents of elemental C and S in the prepared samples were determined by C-S analyser (Eltar, Germany). **The electronic conductivities of the prepared samples were measured by multifunctional digital four-point-probe tester (ST-2258C).**

## Electrochemical tests

The electrochemical **performance of the prepared samples was** evaluated by using CR2025 coin-type cells. The working electrodes were fabricated by mixing 80 wt.% active materials, 10 wt.% acetylene black and 10 wt.% polyvinylidene fluoride as binder. Then the blended powders were putted in N-methyl pyrrolidinone until slurry was obtained. After that, the blended slurry was cast onto a copper current collector, followed by drying at 120 °C for longer than 6 h in vacuum. Following their construction, it was punched to form rounded pieces of area 1.13 cm<sup>2</sup>. The active material on each piece weighs about 2.0 mg. Typically, the film-type cathodes were assembled in a dry Ar-filled glove box using lithium foil as negative electrode, which was separated by a porous polypropylene film from positive electrode, and 1 mol L<sup>-1</sup> LiPF<sub>6</sub> in EC/EMC/DMC (1:1:1 in volume) solvent was used as the electrolyte. At last, the electrochemical tests were carried out via an automatic galvanostatic charge–discharge unit by NEWARE battery circler, between 3.0 and 0.01 V vs. Li<sup>+</sup>/Li electrode at room temperature. The electrochemical impedance spectroscopy (EIS) and cyclic voltammetry measurements (CV) were conducted using CHI660D electrochemical workstation. The impedance spectra were recorded by applying an AC voltage of 5 mV amplitude in the frequency range of 0.01 Hz–100 kHz.

## Calculation methodology

All calculations were performed by using the density functional theory (DFT) with the PBE exchange-correlation functional treated in spin-polarized GGA, as implemented in CASTEP package in Materials studio 7.0. Ultrasoft pseudo potentials (USPP) introduced by Vanderbilt<sup>[12]</sup> have been employed for all ion-electron interactions. The energy convergence criterion for self-consistent field (SCF) calculation was  $1 \times 10^{-6}$  eV/atom. Convergence with respect to both energy cutoff and  $k$ -point mesh was tested. According to the convergence test, an energy cutoff of 500 eV was chosen to ensure that total energies were converged within  $1 \times 10^{-4}$  eV/cell. For the Brillouin zone sampling for bulk and surface material, we carried out  $6 \times 6 \times 4$  and  $6 \times 3 \times 1$   $k$ -points mesh using the method of Monkhorst-Pack.<sup>[13]</sup> To take into account the strong correlation among  $d$  electrons of vanadium ions, the DFT + U method was adopted and a Hubbard-like correlation was added with  $U=3$  eV the appropriated values for vanadium compounds as reported.<sup>[14]</sup>

## Results and discussion

Figure 1 shows the crystal structures of LiVPO<sub>4</sub>F anode materials before and after MoS<sub>2</sub> modification. Both samples possess high-intensity diffraction peaks corresponding to the triclinic structure with P-1 space group.<sup>[7e, 9]</sup> After MoS<sub>2</sub> coating, the M-LVPF sample shows similar peaks' intensities, indicating that the solution coating process of MoS<sub>2</sub> has no obvious effect on the crystal structure of LiVPO<sub>4</sub>F. In addition, for M-LVPF, a small peak is found at the diffraction angle range from 13.0° to 15.5° (green rectangle) which can be ascribed to MoS<sub>2</sub>,<sup>[5e]</sup> which is confirmed by the XRD pattern of as-prepared MoS<sub>2</sub> as shown in Figure S1. Mo3d XPS curve in Figure S2 confirms 2H-MoS<sub>2</sub> is obtained, indicating semiconductor nature of the prepared MoS<sub>2</sub>.

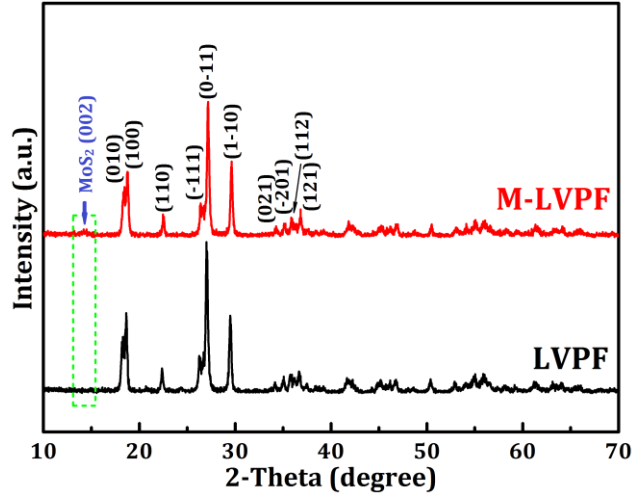


**Figure 1.** XRD patterns of  $\text{LiVPO}_4\text{F}$  before (LVPF) and after (M-LVPF)  $\text{MoS}_2$  modification. The small peak with green rectangle in the XRD curves of M-LVPF is indexed with the lattice plane (002) of  $\text{MoS}_2$ .

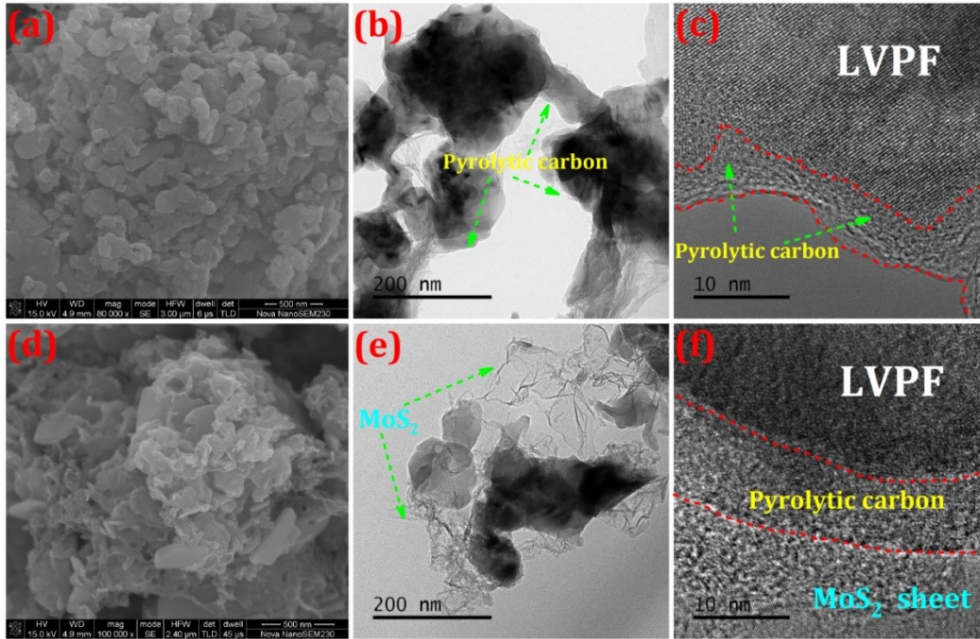


**Figure 2.** (a) SEM, (b) TEM and (c) HRTEM images of LVPF sample; (d) SEM, (e) TEM and (f) HRTEM of M-LVPF sample.

Figure 2(a) and (d) present the SEM images of LVPF and M-LVPF electrodes. It is obvious that the particles of both samples present the similar irregular shapes with a wide



size distribution. Compared to smooth surface of the bare LVPF, M-LVPF shows a rough surface due to MoS<sub>2</sub> coating. From the TEM [Figure 2(b)] and HRTEM [Figure 2(c)] images of LVPF, it can be seen that LiVPO<sub>4</sub>F particles are surrounded by the amorphous carbon. The carbon, weighing to 1.56%, is derived from the excessive amount of oxalic acid. After MoS<sub>2</sub> coating, as shown in Figure 2(e), the LiVPO<sub>4</sub>F crystals in M-LVPF are wrapped by two-dimension (2D) thin-film-like layers, exhibiting a distinguishable boundary between LiVPO<sub>4</sub>F and MoS<sub>2</sub> layers. HRTEM image of M-LVPF [Figure 2(f)] further clearly presents that these LiVPO<sub>4</sub>F nanoparticles are wrapped by amorphous carbon as an interlayer and typical multi-layered MoS<sub>2</sub> as an outer layer. The multi-layered structure can provides an effective conducting network for electronic and ionic transmission during the charge/discharge process. Therefore, such novel multi-layered anode material is able to remain stable performance during cycling process.

The electrochemical performance of LVPF and M-LVPF are evaluated in the potential range of 0.01-3.0 V vs. Li<sup>+</sup>/Li. Figure 3(a) presents the initial discharge-charge curves of LVPF and M-LVPF at 50 mA g<sup>-1</sup>. It is obvious that both samples show the similar cycling curves with the same lithiation plateau at about 1.80 V. In addition, there is a small plateau at ~2.0 V in the charge curve, which is probably attributed to extraction of Li<sup>+</sup> from MoS<sub>2</sub>.<sup>[15]</sup> This phenomenon indicates that the added MoS<sub>2</sub> is able to deliver capacity contribution and it may increase the capacity of M-LVPF. The initial reversible charge capacities of LVPF and M-LVPF are 302 and 308 mAh g<sup>-1</sup>, respectively. Figure 3(b) shows the rate capacity of LVPF and M-LVPF. The bare LVPF electrode shows poor rate capacity, exhibiting the capacity as low as 30 mAh g<sup>-1</sup> when the charge current of 1600 mA g<sup>-1</sup> is applied. While for M-LVPF, as the current increases from 100 mA g<sup>-1</sup> to 1600

$\text{mA g}^{-1}$ , the prepared composite shows some degree of capacity fading from 289 to 199  $\text{mAh g}^{-1}$ , indicating good capacity recovery under the artificially controlled unstable discharge-charge current densities. Moreover, as shown in Figure 3(c), the capacity and rate capacity of M-LVPF is even better than that of graphene-modified  $\text{LiVPO}_4\text{F}$ .<sup>[8b]</sup> Figure 3(d) shows the cycling ability of  $\text{LiVPO}_4\text{F}$  electrodes before and after  $\text{MoS}_2$  coating at the rate of  $1000 \text{ mA g}^{-1}$ . Compared to fast capacity fade of LPVF, M-LVPF shows a horizontal line with cycling going on and no obvious capacity decay. After 300 cycles, LVPF and M-LVPF maintain the capacity retentions of 52.3% and 98.7%, respectively.

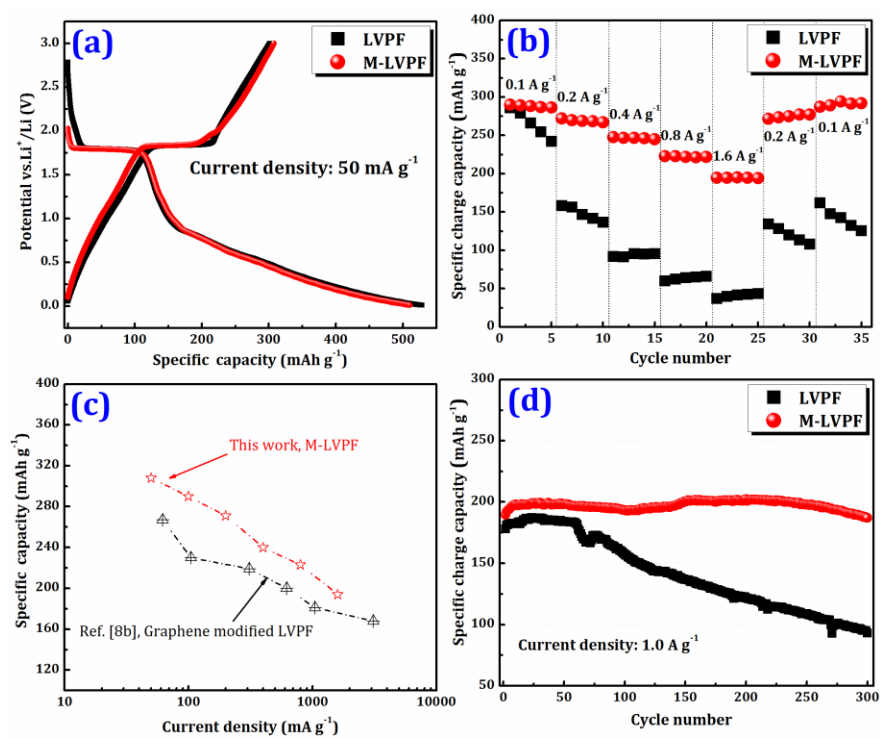


**Figure 3.** (a) Initial discharge-charge profile of LVPF and M-LVPF at  $50 \text{ mA g}^{-1}$ ; (b) Rate capability of LVPF and M-LVPF in the current range of  $50\sim 1600 \text{ mA g}^{-1}$ ; (c) Comparison of capacity retention at different charge-discharge rate between M-LVPF and graphene decorated  $\text{LiVPO}_4\text{F}$ ; (d) Cycle performance of LVPF and M-LVPF at  $1.0 \text{ A g}^{-1}$ .

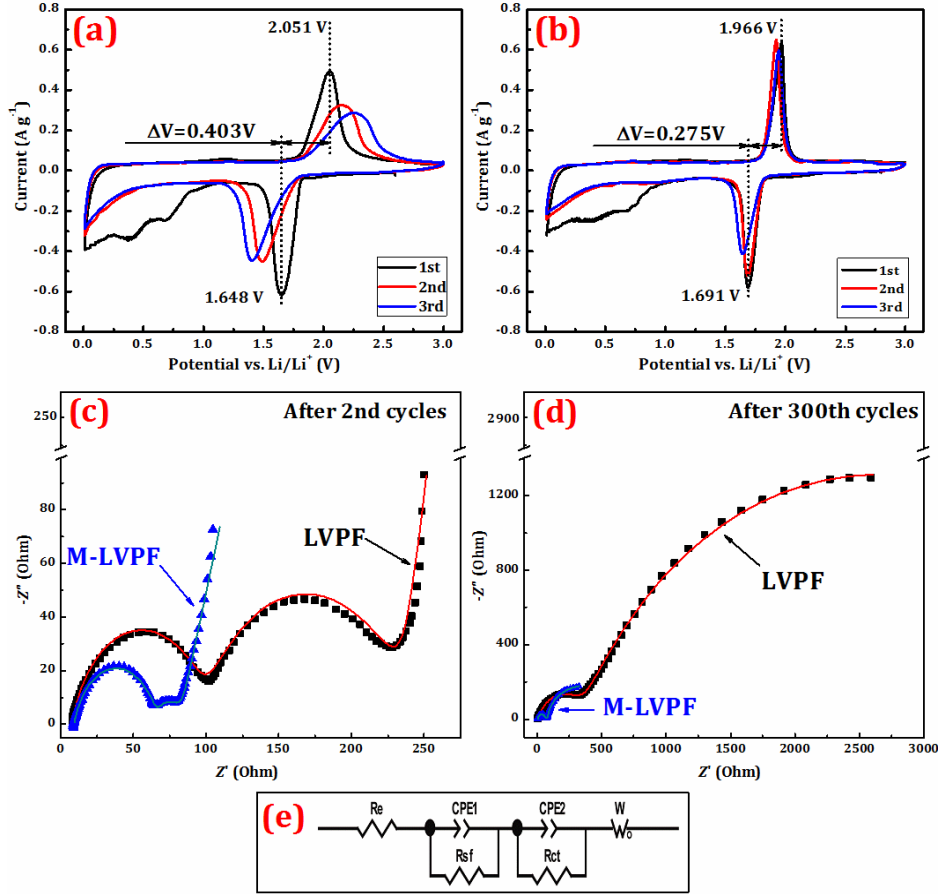


**Figure 4.** CV curves of (a) LVPF and (b) M-LVPF; Nyquist plots of LVPF and M-LVPF after 2 cycles (c) and 500 cycles (d) at 0.01 V vs.  $\text{Li}^+/\text{Li}$ ; (e) Equivalent circuit used to fit the EIS data.

The CV curves of LVPF and M-LVPF in the first three cycles are presented in Figure 4(a) and (b), respectively. In the first cycle, LVPF and M-LVPF display a pair of cathodic/anodic peaks located at around 1.65 and 2.00 V (vs.  $\text{Li}^+/\text{Li}$ ), which are associated with  $\text{Li}^+$  insertion/extraction reactions in the  $\text{LiVPO}_4\text{F}$  crystals, respectively. At lower potential, two wide peaks are found during cathodic scan while no corresponding anodic peak is observed, indicating large irreversibility during the first cycle. This phenomenon may be attributed to irreversible decomposition of the electrolyte and structural degradation of  $\text{LiVPO}_4\text{F}$  within conversion reaction. It is noted that the peaks intensity of M-LVPF at lower potential is much weaker than

that of M-LVPF, indicating M-LVPF shows improved reversibility after MoS<sub>2</sub> coating. When the first cycle completes, the redox reaction becomes stable with reversible lithium extraction/insertion. Therefore, the following two cyclic curves are similar and overlapped. However, the peaks for LVPF after initial cycle shift largely, causing a large polarization, while those for M-LVPF almost located at the initial position. Note that, with MoS<sub>2</sub> modification, the M-LVPF electrode shows decreased anodic peak voltage and increased cathodic peak potential, resulting in a smaller voltage difference (0.275 V) than that for LVPF (0.403 V). These results indicate that the MoS<sub>2</sub> coating layer plays a positive role in improving the **reversibility of the cells during cycling**. Figure 4(c, d) shows the Nyquist plots of LVPF and M-LVPF samples at the discharge state (0.01 V vs. <sup>+</sup>Li/Li) after 2 and 500 cycles, respectively. The profiles of both samples are composed of an intercept and two semicircles. The intercept at high frequency corresponding to the solution resistance ( $R_e$ ) only values several ohms. The first semicircle in high frequency is attributed to the surface film impedance ( $R_{sf}$ ), while the later semicircle emerged in medium frequency represents the charge transfer impedance ( $R_{ct}$ ). For the plots before long-term cycles, as shown in Figure 4(c), the sloping line in the low frequency region is considered as the Warburg impedance ( $W_o$ ), which corresponds to the diffusion of lithium ions in the solid electrode. The impedance spectra are fitted by the equivalent electrical circuit as shown in Figure 4(e) and the main impedance values are listed in Table 1. After battery activating for 2 cycles, the value of  $R_{sf}$  and  $R_{ct}$  of M-LVPF is much smaller than that of the bare LVPF, which is a result of MoS<sub>2</sub> with super structural/chemical stability and good ionic/electronic conductivity, providing a satisfying platform for Li<sup>+</sup> diffusion, electronic transmission and charge-exchange-related reaction at the interface of LiVPO<sub>4</sub>F particles and electrolyte. More importantly, M-LVPF shows much more stable  $R_{sf}$  and  $R_{ct}$  than LVPF within cycling. After 300 cycles, the

values of  $R_{sf}$  and  $R_{ct}$  increase from 91, 136  $\Omega$  to 168, 1961  $\Omega$  for LVPF, and from 57, 15  $\Omega$  to 62, 210  $\Omega$  for M-LVPF, respectively. It indicates that the surface of bare LVPF electrode is heavily damaged by electrolyte. However, with the protection of  $\text{MoS}_2$  coating layer, the surface of M-LVPF is much more stable. All of above support the fact that the  $\text{MoS}_2$ -coated  $\text{LiVPO}_4\text{F}$  delivers much improved electrochemical performance including long-term cycling and rate properties.

**Table 1.** Fitted  $R_{sf}$  and  $R_{ct}$  values of the prepared LVPF and M-LVPF electrode

Cycle number	Bare LVPF		M-LVPF	
	$R_{sf}$ ( $\Omega$ )	$R_{ct}$ ( $\Omega$ )	$R_{sf}$ ( $\Omega$ )	$R_{ct}$ ( $\Omega$ )
2 <sup>nd</sup>	91	136	57	15
300 <sup>th</sup>	168	1961	62	210

To gain further insight into the mechanism of improved electrochemical performance of  $\text{MoS}_2$  coated  $\text{LiVPO}_4\text{F}/\text{C}$ , first-principles calculations are carried out to evaluate the surface properties of  $\text{LiVPO}_4\text{F}/\text{C}$  before and after  $\text{MoS}_2$  coating. Tests of vacuum region of different thickness indicate that adding a 15  $\text{\AA}$  vacuum region on the chapped surface is enough to eliminate the effect from another atom layer. According to Table S1,  $\text{LiVPO}_4\text{F}$  (010) surface exposing Li and O atoms owns the lowest energy and is considered thermodynamically stable. Therefore,  $\text{LiVPO}_4\text{F}$  (010) surface is applied for the calculations of  $\text{MoS}_2$  coating  $\text{LiVPO}_4\text{F}$ . Based on the experimental facts of the lattice plane (001) peak of  $\text{MoS}_2$  in XRD curve (Figure 1) and the existence of amorphous carbon interlayer (Figure 2c and 2f), all the calculations reported here are performed by using (1 $\times$ 2) period slab of  $\text{LiVPO}_4\text{F}$  (010) surface adsorbed with two carbon atoms and a  $\text{MoS}_2$  monolayer, constructing a sandwich structure of  $\text{LiVPO}_4\text{F}$  (010)/C/ $\text{MoS}_2$  (001) (Figure 5a). During all slab calculations, the internal six atom layers (e.g. layer 1-6 of (010) surface in Figure S3) were frozen at bulk positions to simulate the bulk properties of the material,

while the rest of outer layers were allowed to move. The optimized LiVPO<sub>4</sub>F (010) as presented in Figure S3 shows that V atoms in the LiVPO<sub>4</sub>F (010) surface are in the unsaturated state, which have a strong trend to adsorb other atoms to keep stability. Therefore, as shown in Figure 5a, a phenomenon of carbon atoms bonding to these unsaturated V atoms was observed. There is a layer interface between the LiVPO<sub>4</sub>F (010) surface and the MoS<sub>2</sub> monolayer, indicating the interaction between them is the weak van der Waals (vdW) force. Interestingly, two sulphur atoms disaffiliate from the MoS<sub>2</sub> monolayer and form a chemical bond with carbon atom to reduce its unsaturation, producing sulphur vacancy defects in MoS<sub>2</sub> monolayer. This supports the fact that MoS<sub>2</sub> can significantly decrease the activity of carbon-modified-LiVPO<sub>4</sub>F surface and thereby provide a stable surface for electrochemical reactions. As a result, the cycling performance of M-LVPPF is much improved. The strength of interfacial interaction can also be identified from the adsorption energy ( $E_a$ ), which is defined as follows:

$$E_a = E_{\text{surface with MoS}_2} - E_{\text{MoS}_2} - E_C - E_{\text{clean surface}} \quad (1)$$

where  $E_{\text{surface with MoS}_2}$ ,  $E_{\text{MoS}_2}$ ,  $E_C$  and  $E_{\text{clean surface}}$  are the DFT total energy of the surface with MoS<sub>2</sub>, MoS<sub>2</sub> (001) monolayer, carbon atom and clean LiVPO<sub>4</sub>F (010) surface, respectively. The calculated surface adsorption energy of LiVPO<sub>4</sub>F (010)/C/MoS<sub>2</sub> (001) system is -2.53 eV/MoS<sub>2</sub> molecule, further verifying the stability of LiVPO<sub>4</sub>F (010) surface absorbed with carbon and MoS<sub>2</sub> monolayer. It also indicates that the process of MoS<sub>2</sub> adsorbing carbon-modified-LiVPO<sub>4</sub>F is exothermic and spontaneous. Figure 5b shows the electron density difference of LiVPO<sub>4</sub>F (010)/C/MoS<sub>2</sub> (001) system. An increased electron density is observed between V-C and C-S bond, which represents the strong covalent interaction, increasing the stability of LiVPO<sub>4</sub>F (010) after surface coating. In addition, the negligible charge transfer at the interface between the carbon-

adsorbed-LiVPO<sub>4</sub>F (010) surface and the MoS<sub>2</sub> monolayer suggests that the non-covalent interactions play an important role in determining the interfacial interaction of LiVPO<sub>4</sub>F (010)/C/MoS<sub>2</sub> (001) system. To evaluate the change of electron conductivity of carbon-modified-LiVPO<sub>4</sub>F (010) surface system after MoS<sub>2</sub> coating, the total density of states (DOS) and partial density of states (PDOS) of LiVPO<sub>4</sub>F (010)/C and LiVPO<sub>4</sub>F (010)/C/MoS<sub>2</sub> (001) system are depicted in Figure 5c and 5d, respectively. Viewed from Figure 5c, for LiVPO<sub>4</sub>F (010)/C system the quantum state near the Fermi level is absolutely dominated by the V-3*d* state. Compared to the DOS of clean LiVPO<sub>4</sub>F (010) (Figure.S4), it can be seen that adsorbed carbon slightly increase the electron state near the Fermi level. However, after MoS<sub>2</sub> coating on the LiVPO<sub>4</sub>F (010)/C surface, the introduced 2*p* state of S atom and 3*d* state of Mo atom change the PDOS a lot (Figure 5d) and significantly increase the electron states near the Fermi level (Figure 5e). Generally, the electrical conductivity of a system is proportional to the electron state near the Fermi level. Moreover, overlap of 2*p* state of C and S1 atom is observed, demonstrating the covalent interaction of C-S bond. Thus, a conclusion can be made that MoS<sub>2</sub> coating is able to enhance the electronic conductivity of LiVPO<sub>4</sub>F/C. The electronic conductivity of LVPF and M-LVPF determined by four-point-probe method are  $1.95 \times 10^{-3}$  and  $9.42 \times 10^{-3}$  S m<sup>-1</sup>, respectively, further verifying the enhanced electronic conductivity of M-LVPF. The increased conductivity is beneficial to the rate performance of MoS<sub>2</sub>-coated LiVPO<sub>4</sub>F materials. Considering the fact that the carbon would not be completely and homogenously covered on the surface of LiVPO<sub>4</sub>F and thereby the MoS<sub>2</sub> can be directly contacted with carbon (at the surface coated with carbon) or LiVPO<sub>4</sub>F (at the surface without carbon coating), the calculation for MoS<sub>2</sub> adsorbing LiVPO<sub>4</sub>F (010) surface

without carbon layer is also performed. The results in Figure S5 also indicate this process is exothermic and spontaneous, and the enhanced conductivity can be obtained. Therefore, these theoretical calculations well explain the mechanism for improved electrochemical performance of M-LVPF.

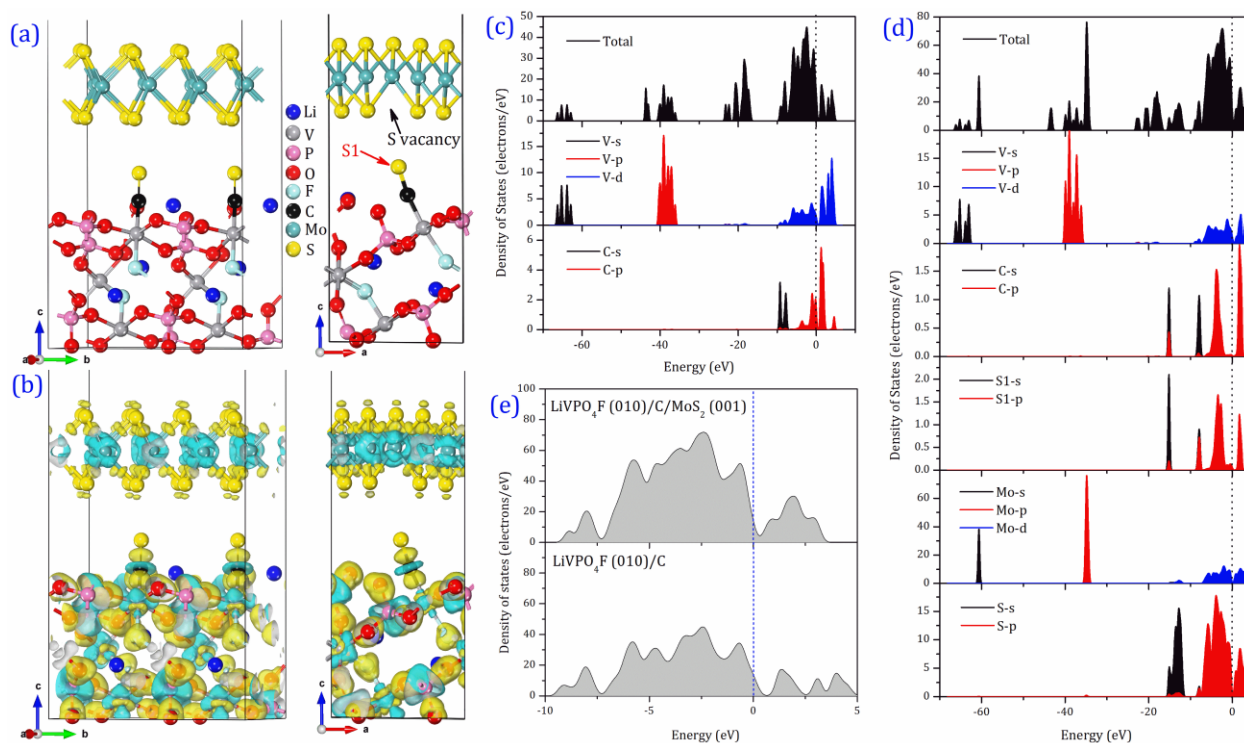


Figure 5 (a) Relaxed (1×2) slab model of the LiVPO<sub>4</sub>F (010)/C/MoS<sub>2</sub> (001) system; (b) Electron density difference of LiVPO<sub>4</sub>F (010)/C/MoS<sub>2</sub> (001) system, which is visualized by an iso-surface value of 0.1 eV Å<sup>-3</sup>; the yellow color represents increased charge density and the blue color denotes depleted charge density; (c) Total DOS and PDOS of LiVPO<sub>4</sub>F (010)/C system; (d) Total DOS and PDOS of LiVPO<sub>4</sub>F (010)/C/MoS<sub>2</sub> (001) system; (e) Comparison of total DOS of LiVPO<sub>4</sub>F (010)/C and LiVPO<sub>4</sub>F (010)/C/MoS<sub>2</sub> (001) system, where the Fermi energy is shifted to 0 eV.



## Conclusions

In this contribution, MoS<sub>2</sub> modified LiVPO<sub>4</sub>F/C composite was synthesized through a solution method followed by low-temperature calcination to improve the performance of LiVPO<sub>4</sub>F anode. In the designed architecture, LiVPO<sub>4</sub>F particles were wrapped by amorphous carbon as an interlayer and MoS<sub>2</sub> layers as an external surface. Such MoS<sub>2</sub>-modified LiVPO<sub>4</sub>F used as anode delivered superior electrochemical performance including long-life cycle and remarkable rate capacity. First-principles calculations proved that the process of MoS<sub>2</sub> adsorbing with LiVPO<sub>4</sub>F was exothermic and spontaneous, and the electron transfer property of the MoS<sub>2</sub>-modified LiVPO<sub>4</sub>F surface was enhanced. It was believed that MoS<sub>2</sub> coating layer brought two major aspects of benefits. One was to stabilize the surface of LiVPO<sub>4</sub>F particles; the other was to increase the surface conductivity. The theoretical results are well consistent with the electrochemical performance of MoS<sub>2</sub>-coated LiVPO<sub>4</sub>F. As a whole, this work provided the train of thought to develop LiVPO<sub>4</sub>F as a novel anode material and to exploit MoS<sub>2</sub> as a promising and general coating material.

## Acknowledgment

This work is supported by National Natural Science Foundation of China (Grant No. 51574287) and the Fundamental Research Funds for the Central Universities of Central South University. We also thank the Advanced Research Centre of CSU for performing HRTEM examination. The corresponding author appreciates the supporting from Baosteel Education Fund.

## References

- [1] S. F. Tie, C. W. Tan, *Renew. Sust. Energy Rev.* **2013**, *20*, 82-102.

- [2] a) L. Mai, X. Tian, X. Xu, L. Chang, L. Xu, *Chem. Rev.* **2014**, *114*, 11828-11862; b) R. H. Wang, X. H. Li, Z. X. Wang, H. J. Guo, Z. J. He, *ACS Appl. Mater. Interfaces* **2015**, *7*, 23605-23614; c) M. Armand, J.-M. Tarascon, *Nature* **2008**, *451*, 652-657.
- [3] a) J. Wang, Q. Zhang, X. Li, D. Xu, Z. Wang, H. Guo, K. Zhang, *Nano Energy* **2014**, *6*, 19-26; b) T. Li, X. H. Li, Z. X. Wang, H. J. Guo, Y. Li, *J. Mater. Chem. A* **2015**, *3*, 11970-11975; c) N. Nitta, F. Wu, J. T. Lee, G. Yushin, *Mater. Today* **2015**, *18*, 252-264.
- [4] a) F. Ding, W. Xu, D. Choi, W. Wang, X. Li, M. H. Engelhard, X. Chen, Z. Yang, J.-G. Zhang, *J. Mater. Chem.* **2012**, *22*, 12745; b) F. Wu, X. Li, Z. Wang, H. Guo, Z. He, Q. Zhang, X. Xiong, P. Yue, *J. Power Sources* **2012**, *202*, 374-379; c) H. Kim, G. Jeong, Y. U. Kim, J. H. Kim, C. M. Park, H. J. Sohn, *Chem. Soc. Rev.* **2013**, *42*, 9011-9034; d) M.-L. Lee, Y. H. Li, S.-C. Liao, J.-M. Chen, J.-W. Yeh, H. C. Shih, *Electrochim. Acta* **2013**, *112*, 529-534.
- [5] a) H. B. Wu, J. S. Chen, H. H. Hng, X. W. D. Lou, *Nanoscale* **2012**, *4*, 2526-2542; b) J. Wang, Q. Zhang, X. Li, B. Zhang, L. Mai, K. Zhang, *Nano Energy* **2015**, *12*, 437-446; c) Q. Zhang, J. Wang, J. Dong, F. Ding, X. Li, B. Zhang, S. Yang, K. Zhang, *Nano Energy* **2015**, *13*, 77-91; d) F. Xiong, Z. Cai, L. Qu, P. Zhang, Z. Yuan, O. K. Asare, W. Xu, C. Lin, L. Mai, *ACS Appl. Mater. Interfaces* **2015**, *7*, 12625-12630; e) J. Zhou, J. Qin, X. Zhang, C. Shi, E. Liu, J. Li, N. Zhao, C. He, *ACS Nano* **2015**, *9*, 3837-3848; f) J. Zai, K. Wang, Y. Su, X. Qian, J. Chen, *J. Power Sources* **2011**, *196*, 3650-3654.
- [6] a) K. Evanoff, A. Magasinski, J. Yang, G. Yushin, *Adv. Energy Mater.* **2011**, *1*, 495-498; b) H. T. Nguyen, M. R. Zamfir, L. D. Duong, Y. H. Lee, P. Bondavalli, D. Pribat, *J. Mater. Chem.* **2012**, *22*, 24618; c) H. Mukaibo, T. Momma, M. Mohamedi, T. Osaka, *J.*

- Electrochem. Soc.* **2005**, *152*, A560-A565; d) M. N. Obrovac, V. L. Chevrier, *Chem. Rev.* **2014**, *114*, 11444-11502.
- [7] a) X. Sun, Y. Xu, M. Jia, P. Ding, Y. Liu, K. Chen, *J. Mater. Chem. A* **2013**, *1*, 2501-2507; b) Y. Piao, C.-k. Lin, Y. Qin, D. Zhou, Y. Ren, I. Bloom, Y. Wei, G. Chen, Z. Chen, *J. Power Sources* **2015**, *273*, 1250-1255; c) Z. Liu, W. Peng, K. Shih, J. Wang, Z. Wan, H. Guo, G. Yan, X. Li, L. Song, *J. Power Sources* **2016**, *313*, 65-72; d) J.-c. Zheng, B. Zhang, Z.-h. Yang, *J. Power Sources* **2012**, *202*, 380-383; e) B. Zhang, Y.-d. Han, J.-c. Zheng, C. Shen, L. Ming, J.-f. Zhang, *J. Power Sources* **2014**, *264*, 123-127; f) R. Ma, L. Shao, K. Wu, M. Shui, D. Wang, N. Long, Y. Ren, J. Shu, *J. Power Sources* **2014**, *248*, 874-885; g) J.-c. Zheng, Y.-d. Han, B. Zhang, C. Shen, L. Ming, J.-f. Zhang, *ACS Appl. Mater. Interfaces* **2014**, *6*, 13520-13526.
- [8] a) R. Ma, L. Shao, K. Wu, M. Shui, D. Wang, J. Pan, N. Long, Y. Ren, J. Shu, *ACS Appl. Mater. Interfaces* **2013**, *5*, 8615-8627; b) J. Wang, X. Li, Z. Wang, B. Huang, Z. Wang, H. Guo, *J. Power Sources* **2014**, *251*, 325-330; c) J. Barker, R. K. B. Gover, P. Burns, A. Bryan, *Electrochem. Solid-State Lett.* **2005**, *8*, A285-A287; d) L. S. Plashnitsa, E. Kobayashi, S. Okada, J.-i. Yamaki, *Electrochim. Acta* **2011**, *56*, 1344-1351.
- [9] B. L. Ellis, T. N. Ramesh, L. J. M. Davis, G. R. Goward, L. F. Nazar, *Chem. Mater.* **2011**, *23*, 5138-5148.
- [10] a) Y. Shi, J. Wang, C. Wang, T. T. Zhai, W. J. Bao, J. J. Xu, X. H. Xia, H. Y. Chen, *J. Am. Chem. Soc.* **2015**, *137*, 7365-7370; b) Haotian Wang, Z. Lu, D. Kong, J. Sun, T. M. Hymel, Y. Cui, *ACS Nano* **2014**, *8*, 4940-4947; c) G. Eda, H. Yamaguchi, D. Voiry, T. Fujita, M. Chen, M. Chhowalla, *Nano Lett.* **2011**, *11*, 5111-5116; d) D. Voiry, M. Salehi, R. Silva, T. Fujita, M. Chen, T. Asefa, V. B. Shenoy, G. Eda, M. Chhowalla, *Nano Lett.* **2013**, *13*,

- 6222-6227; e) Y. Wang, D. Chen, X. Yin, P. Xu, F. Wu, M. He, *ACS Appl. Mater. Interfaces* **2015**, *7*, 26226-26234.
- [11] Y. Fan, Z. Liu, Q. Hun, X. Li, Z. Wang, H. Guo, J. Wangn, *Ceram. Int.* **2015**, *41*, 13891-13895.
- [12] R. C. Kari Laasonen, Changyol Lee, David Vanderbilt, *Phys. Rev. B* **1991**, *43*, 6796-6799.
- [13] a) H.J. Monkhorst, J. D. Pack, *Phys. Rev. B* **1976**, *13*, 5188-5192.
- [14] a) Y. Li, B. Huang, X. Cheng, Y. Zhang, *J. Electrochem. Soc.* **2015**, *162*, A787-A792; b) M. M. Islam, M. Wilkening, P. Heitjans, T. Bredow, *J. Phys. Chem. Lett.* **2012**, *3*, 3120-3124.
- [15] T. Stephenson, Z. Li, B. Olsen, D. Mitlin, *Energy Environ. Sci.* **2014**, *7*, 209-231.

Graphical Abstract